Journal of Manufacturing Processes 125 (2024) 253–266

Contents lists available at ScienceDirect

Journal of Manufacturing Processes

journal homepage: www.elsevier.com/locate/manpro

Modelling of an innovative cryogenic assisted dieless sheet metal piercing process

Paolo Albertelli *, Michele Monno

Mechanical Engineering Department, Politecnico di Milano, via la Masa 1, 20156 Milan, Italy
Consorzio MUSP, via Callegari, 29122 Piacenza, Italy

ARTICLE INFO

Keywords:
Piercing
Punching
Cryogenic
Constitutive models
FEM simulations
Ductile-to-brittle transition

ABSTRACT

In tube piercing, if the internal die is necessary to properly pierce the tube avoiding its crushing, it also represents a bottleneck to a rapid change of the piercing/punching set. In this research, an innovative dieless tube piercing approach has been conceived and studied. The use of a cryogenic fluid to force the material ductile-brittle transition is a way to limit the sheet deformation during the dieless piercing process. The analysis of the innovative cryogenic piercing process was carried out both adopting numerical and experimental methodologies. A finite element FE model of the cryogenic piercing was developed and updated in two stages. First, experimental tensile tests, performed at cryogenic temperatures, were used to characterize some material properties. Secondly, some piercing tests in cryogenic conditions were carried out at different velocities and temperatures to fine update the model. A validation session was executed to assess the model and the process feasibility. It was found that the FE model reproduced the experimental results within a maximum estimation error of 10 % on both the required piercing force and on the deviation from the nominal dimension of the tube cross-section. Although the piercing tests were conducted at quite a low temperature (−80 °C), an extended analysis of the wall fractures confirmed that a proper ductile-to-brittle transition did not occur. Further increasing the punching velocity and especially decreasing the piercing temperature could be the only viable solutions to promote the transition and further reduce tube deformation.

Introduction

The use of cryogenic fluids in manufacturing processes represents a rather new research branch. Jawahir et al. in [1] critically reviewed the main applications in which cryogenics is used in manufacturing and outlined the most relevant opportunities and challenges in the field.

One of the most studies areas has been the machining of difficult to cut materials. Cryogenic fluids are used as alternative coolants for increasing productivity and extending the life of the cutting tools. Few relevant reviews on cryogenic-assisted cutting can be found in the specific literature [2,3]. For instance, Shokrani et al. in [4] reported the main achieved results considering both different materials and cutting processes. The authors analysed the research results in terms of enhancements of the processed surface integrity: roughness, hardness, residual stresses, and metallurgic properties. Most of the literature findings came from experimental activities, typically performed in laboratory conditions. In [5,6], the authors specifically focused their reviews on cryogenic machining of titanium alloys. The potentialities of cryogenics in metal cutting have been investigated especially from the environmental sustainability perspective, [7–11]. Gupta and Laubscher [12] carried out a review on this topic. Despite its great potentialities, cryogenics still has not been widely adopted in metal cutting industries since it was observed that the increment of the performances was not consistent and robust with respect to the adopted experimental conditions. Moreover, a lack of full comprehension of all the involved phenomena affects a feasible exploitation of the technology in shopfloors. To bridge this gap, recently, a more massive usage of models (e.g., for the tribological behaviour, for modelling the thermo-mechanics interactions or to estimate the cooling action) has been introduced, [13–18].

One of the most relevant challenges in this field remains the description of the material behaviour in process-induced conditions. Indeed, almost all the research on cryogenics was focused on the material characterization in these extreme temperature conditions, [19,20]. If some metallic materials properties (wear resistance, tensile strength, thermal and electrical conductivity) are enhanced by low

* Corresponding author at: Mechanical Engineering Department, Politecnico di Milano, via la Masa 1, 20156 Milan, Italy.
E-mail address: paolo.albertelli@polimi.it (P. Albertelli).

https://doi.org/10.1016/j.jmapro.2024.07.065
Received 4 August 2023; Received in revised form 31 May 2024; Accepted 17 July 2024
Available online 19 July 2024

temperatures, other features (e.g., ductility) can differently be affected by cryogenics. For instance, in materials with face-centered cubic (fcc) lattice, the ductility is kept even at low temperatures whereas in body-centered cubic (bcc) and hexagonal-closed packed (hcp), the ductile-to-brittle transition occurs, [1]. Several research works on the micro-structural analysis were carried out to better understand the origin of such different behaviours, e.g., [21]. Some works on modelling were accomplished, e.g., [22].

The temperature-dependent material properties have been exploited in many applications and manufacturing processes. Cryoprocessing of steel, due to the formation of carbides and a higher martensite content, assures an improved hardness and fatigue life of the treated components, [23]. In [24,25], the deep cryogenic treatment DCT was used to maximize the life extension of 100Cr6 bearings. This treatment has been widely exploited in metal cutting and forming processes to protract the duration of the tools. For instance, [26,27] analysed the performances of metal cutting tools while [28,29] focused on tool for stamping and punching. Even the high deformability of some aluminium alloys at cryogenic temperatures has been exploited to ease metal forming processes. Yang et al. [30] experimental investigated the drawability enhancement at low temperatures. Wan et al. in [31] studied the forming limit of tubes with a cryogenic set-up, [31].

Regarding the ductile-to-brittle transition, several research works were carried out. It was found that a transition temperature characterizes this phenomenon, [32] and that the transition occurs even at low loading rates. Some works [33,34] observed an increment of the transition temperature associated to the increment of the strain rate although very high values are typically required to observe substantial effects on the stress. The effects of impurities and of the grain size were also studied. Specifically, it was found that the higher the impurities the higher the transition temperature. Conversely, the lower the grains size the lower the transition temperature, [35].

Although a lot of knowledge on ductile-to-brittle transition and on the materials behaviour at cryogenic temperatures has been developed, this material feature has not yet been positively exploited in manufacturing processes. Indeed, only few works have been found. For instance, with reference to artificial tissue scaffold, Sagar et al. in [36] conceived an innovative micro-piercing process on polycaprolactone in cryogenic condition to exploit the glass transition of the silicon. Specifically, in [37] Sagar et al. arranged some compressive tests to identify the material behaviour in cryogenic temperature and developed a Finite Element model to predict the piercing force. The proposed material modelling is rather simplified since only the influence of the strain was considered. Indeed, the effects of the temperature and of the strain rate were not considered. In [38] it was found that the model can predict the piercing force quite accurately although the validation procedure was rather limited. Moreover, the present paper deals with a different application (steel piercing) and it proposes an additional challenge linked to the absence of the supporting die. Mizumura et al. in [39] proposed a dieless piercing process for hydroformed components. Although in this application the die was not used, the piercing was eased by a high inner pressure that support the sheet of metal.

To bridge this gap, the present study investigates the possibility of exploiting the ductile-to-brittle transition to perform dieless piercing with restrained tube deformation. The novelty of this research is associated to the development of a piercing model that can be used to robustly estimate the required punching/piercing force and the tube deformation according to the specific adopted process parameters and cryogenic conditions. Moreover, a critical analysis of the material behaviour during the dieless piercing was carried out and reported.

The paper is structure as follows. In the Material and Methods section, a first process description was provided. The features of the models, both considering the finite element FE modelling and the material rheological behaviour were reported. The strategy to update the model and the design of experiments were also presented in a specific section. The Results and Discussion section presents the main experimental findings. Moreover, a proper validation of the conceived modelling approach was provided. Final considerations on the material behaviour occurred during the tests and on the achieved results were also reported.

Materials and methods

In this paper section, a description of the innovative dieless cryogenic tube piercing process is provided. A conceptual comparison between the regular tube punching process and the cryogenic dieless punching is reported in Fig. 1 a) and c). Since some materials show a ductile-to-brittle transition at cryogenic temperatures, the possibility to pierce a tube without the internal die (Fig. 1 b)) but, at the same time, restrained the sheet deformation has been investigated, Fig. 1 c). The first implementation of the cryogenic piercing process was depicted in Fig. 1 d). It is worth of noting that the tube is cooled by an inner flow of liquid nitrogen LN. The tube is hold by the bottom part of the external die while the punch and the upper part of the die can move vertically to allow the tube feed after the piercing execution. In this specific cryogenic piercing release, a 30 mm × 30 mm tube of S235JR (welded after roll forming) steel with a thickness of 2.4 mm was adopted. The punch diameter is equal to 10 mm. Additional information on the experimental set-up are provided in the Design of Experimental section.

In the following subsections details regarding the model development, calibration and validation procedures are provided.

Finite element modelling

In this research it was decided to model the novel cryogenic process through a finite element FE approach. The goal of the model is to predict both the tube deflection and the required force in dieless cryogenic piercing. It can be considered a useful tool for setting the specifications (in terms of piercing velocity and requested force) of a new cryogenic piercing machine. The capability of predicting the tube deflection is of paramount relevance since it can be used for check if the specification in term of tube quality can be achieved.

The FE model was developed in ForgeNxT2.1. Three-dimensional finite elements (tetrahedrons with five nodes and linear interpolation) were used for meshing the punch and the tube. The implemented formulation allows considering both the deformation mechanics and thermal equations. With respect to a standard 4-nodes tetrahedron, the adopted element has an additional node, called “bubble node”, placed at the centroid of the tetrahedron. Three kinematic degrees of freedom for each node were considered [36]. The bubble node is used to divide the initial tetrahedron into 4 sub-tetrahedra by joining this node to each of the facets of the initial tetrahedron [37]. An implicit integration scheme, with the Newton-Raphson method was used.

An overview of the dieless punching process model and its main settings was reported in Fig. 2. The mesh size was refined in three specific regions as reported in Fig. 2 b) and Table 1. It was decided to model the punch as a rigid body since the deformation is mostly related to the tube. Even the tube supports (external equipment) were modelled as rigid bodies.

In accordance with the experimental set-up, the punch stroke was set equal to 8 mm. The punch velocity v_p was considered constant during the punching. The range of 4-140 mm/s for the punching velocity was considered for the simulations. An upper threshold for the punching force F_{sim} was imposed to reproduce the pressure limitations associated to the hydraulic units used for driving the punch. Indeed, if the resulting punching force overcomes the threshold, the simulation is quitted. Regarding the punching temperature T_p, according to the described implementation of the cryogenic process (Fig. 1), it was set uniformly into the whole tube while the punch temperature was set equal to the environmental temperature (20 °C).

The heat exchange between the tube and the punch/environment was limited since a steady state punching temperature was assured by a calibrated flow of liquid nitrogen inside the tube.

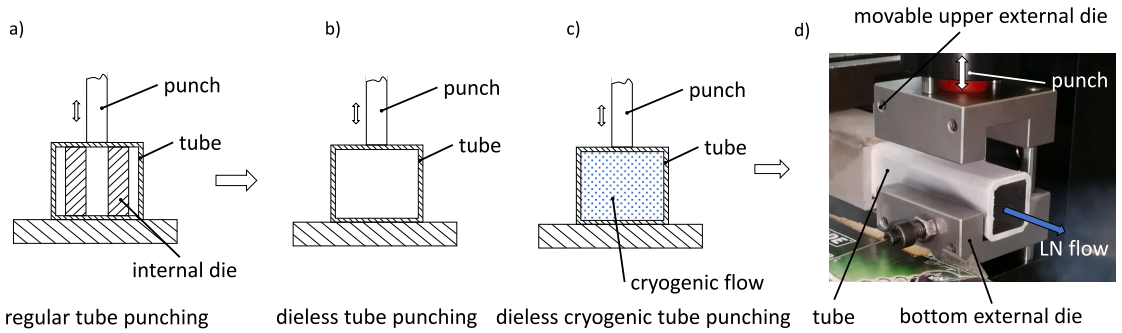

Fig. 1. a) regular tube punching/piercing scheme b) dieless tube punching/piercing scheme c) cryogenic punching/piercing scheme d) cryogenic experimental set up.

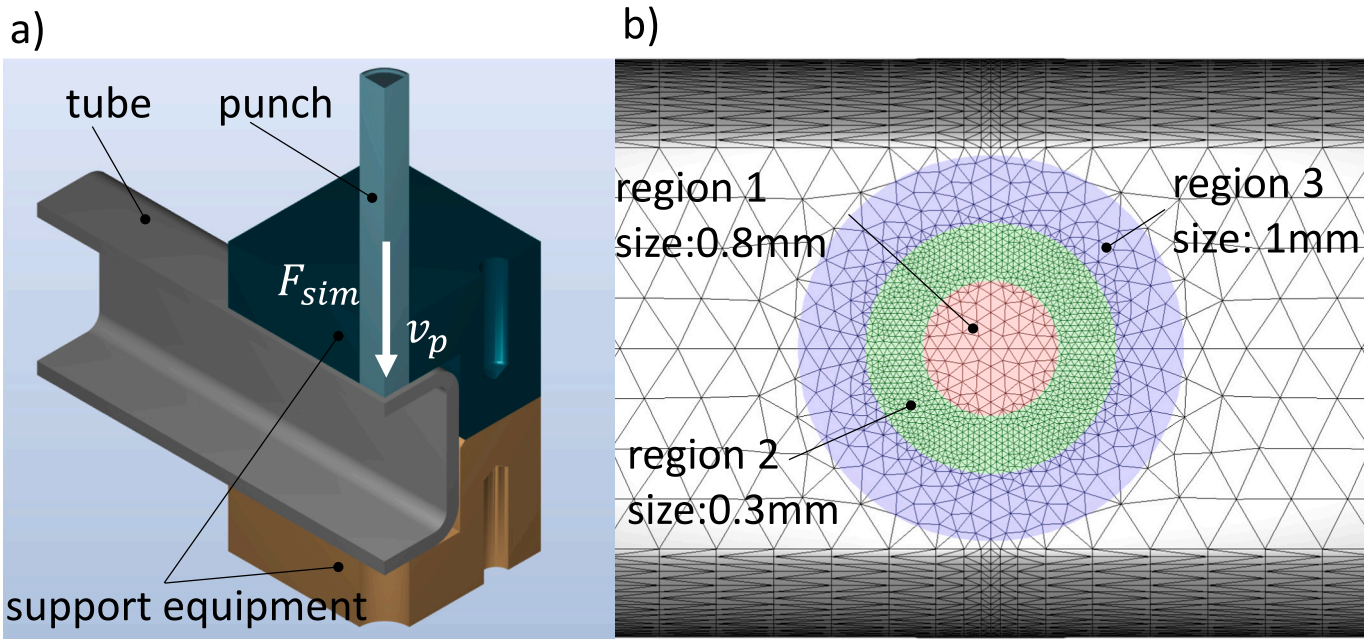

Fig. 2. a) dieless tube piercing modelling b) mesh regions.

Table 1
Mesh properties.

Region	Inner diameter [mm]	Outer diameter [mm]	Mesh size [mm]
1	0	7	0.8
2	7	13	0.3
3	13	20	1

For what concerns the punch-tube contact, the chosen friction model was a stick-slip Coulomb-Tresca model (Eq. (1)). μ is the friction coefficient, m_f the friction factor, τ the shear stress, σ_n the normal pressure and τ_{lim} the yield shear stress which depends on the material flow stress σ according to Von-Mises.

$$\begin{aligned} \tau &= \mu \bullet \sigma_n \quad \text{when } \mu \bullet \sigma_n < m_f \bullet \tau_{lim} \\ \tau &= m_f \bullet \tau_{lim} \quad \text{when } \mu \bullet \sigma_n \geq m_f \bullet \tau_{lim} \end{aligned} \tag{1}$$

In the developed model, the following values were adopted $\mu = 0.4$; $m_f = 0.8$.

The friction value was selected according to the suggestions provided in [40]. Since the piercing tests were conducted without any lubricant, the upper bound of the suggested values was assumed.

Material modelling

It was decided to adopt the basic Johnson-Cook (JC) formulation that has been profitably used both in machining [41] and forming processes [42], Eq. (2)

$$\sigma = (A + B\varepsilon^n)(a + C \bullet ln(\dot{\varepsilon}/\varepsilon_0))\left(1 - \left(\left(T_p - T_0\right)/T_m - T_0\right)^m\right) \tag{2}$$

σ is the flow stress, $\dot{\varepsilon}$ the strain rate, T_p, T_m and T_0 are respectively the piercing temperature, the melting temperature and a temperature used as the reference. A is the initial yield stress, B allows considering the material hardening phenomenon, n is the index associated to the strain sensitivity, C is the index that considers the dependency due to the strain rate, $\dot{\varepsilon}_0$ is the reference value for the strain rate and m is the coefficient that considers the temperature dependency. The innovative aspect of the present study is related to the characterization of the material behaviour at the cryogenic temperatures. Thus, a strategy for the model parameters identification was conceived, refer to the section Model Updating Strategy. For what concerns the damage modelling, it was decided to adopt the Latham-Cockcroft LC formulation (Eq. (3)) that is the most established approach for modelling fracture after large strain deformation.

$$D = \int_0^{\varepsilon_f} \sigma_1 d\varepsilon \tag{3}$$

D is the threshold value that is used for eliminating the damaged elements during the simulations, σ_I is the highest principal component of the stress tensor, and ε_f is the limit fracture strain. More specifically, the critical damage value is calculated for each element under deformation at each time-step. Once the damage value in an element reaches the critical one, a crack is initiated in two steps: (i) this element is deleted with all the parameters related to it, including element connectivity definition, the strain and stress values; (ii) the rough boundary produced by element deletion is smoothed by cutting out the considered rough angle and adding new points.

Model simulations and settings

The developed model was used to simulate the dieless piercing/punching process. More in details, the tube deformation d_t (including the maximum value $d_{t,max,sim}$), the stress and the strain distribution and the punching force F_{sim} (including its maximum value $F_{sim,max}$) were estimated. To limit the effect of numerical oscillations in the computation of the maximum values, the forces were processed through a moving average algorithm, see Fig. 3 c). For sake of example, some simulation outputs were shown in Fig. 3 a) and b) and c).

Model updating strategy

An overview of the model settings described in the previous sections was reported in Fig. 4 a). Moreover, some preliminary information about the performed experimental activities and the associated data used for updating the model were provided. Specifically, tensile tests (stress as a function of strain) at different temperatures were carried out to partially update the JC material model. Conversely, the material damage modelling was updated using the force and the tube deformation data extracted from cryogenic piercing tests, performed at different temperatures and velocities. Other piercing tests were used for the final model validation.

The procedure for updating both the material and the damage models was summarized in Fig. 4 b). For what concerns the Johnson-Cook model parameters, the following approach was adopted. A, B, n were identified from quasi-static test (tensile tests) at the reference temperature (−80 °C). The tensile tests were executed considering a reference strain rate ($\dot{\varepsilon}_0 = 0.002/s$) to neglect the strain rate effect. The adopted conditions also allowed neglecting the temperature related term. Three specimens were used, and the average nominal stress-strain curve was computed for the identification process. The approach suggested in Schwab and Harter [43] was adopted to estimate the true stress strain curve $\sigma = f(\varepsilon)$ from the corresponding nominal quantities (s and e).

The identification of the parameters was twofold. First, the A parameter was identified as the initial yielding stress. In the second step, a regression procedure performed on the tensile test data corresponding to the homogeneous plastic deformation region, thus excluding both the elastic and necking region, was carried out for the identification of B and n.

m is calculated using the results of tests (tensile tests) at different temperatures. (−80 °C, −60 °C, −40 °C). For each temperature T_p, the stress σ data associated to different strain values ($\varepsilon_1 = 0.1, \varepsilon_2 = 0.15, \varepsilon_3 = 0.2$) were used. Starting from the JC formulation and introducing $K = (A + B\varepsilon^n)$, the following relationships (Eq. (4)) can be obtained:

$$ln(1 - \sigma/K) = m \bullet ln\big((T_p - T_0)/(T_m - T_0)\big) \quad (4)$$

As a result, the identification of the m parameter was done through a linear regression of the experimental data. See Results and discussion session, Table 3.

C is updated comparing the results (simulations and experimental data) of the piercing tests in terms of cutting forces (F_{max}). In Fig. 3 c) an example of the simulated piercing force was reported. This updating approach was used to characterize the contribution of the strain rate in realistic conditions that are not achievable through tensile tests since the feed velocity of the tensile machine crossbar is generally rather limited. Additional details on the experimental force measurements were provided in the next paper session.

Regarding the LC model parameter D, in this work, it was decided to characterize the material damaging considering the combined effect of temperature and strain rate. To accomplish it, a procedure based on experimental punching tests performed at different piercing temperatures T_p and different piercing velocities v_p was adopted. As a result, the formulation of the LC model can be resumed as $D = D(v_p, T_p)$. According to what reported in Fig. 4 b), for each tested condition, the FE model was updated, properly tuning the D parameter, to get the experimental maximum tube deflection $d_{t,max}$. Additional details on experimental measurement of the tube deflection were provided in the next sections.

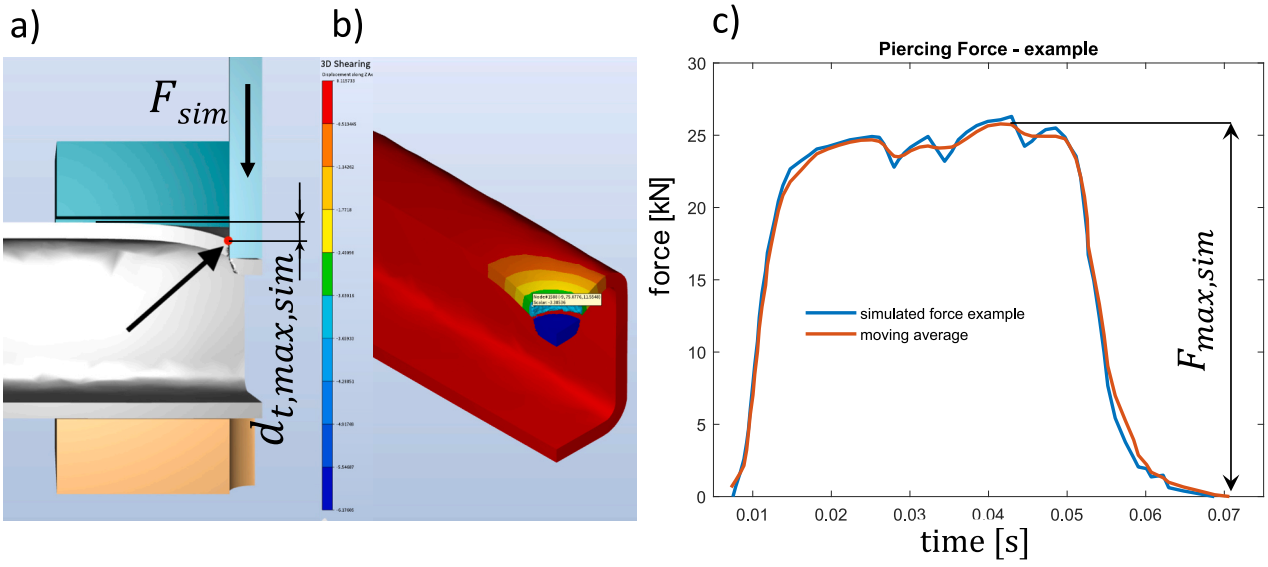

Fig. 3. Example of FE model simulations a) maximum tube deflection estimation $d_{t,max,sim}$ b) deformation map c) piercing force $F_{max,sim}$.

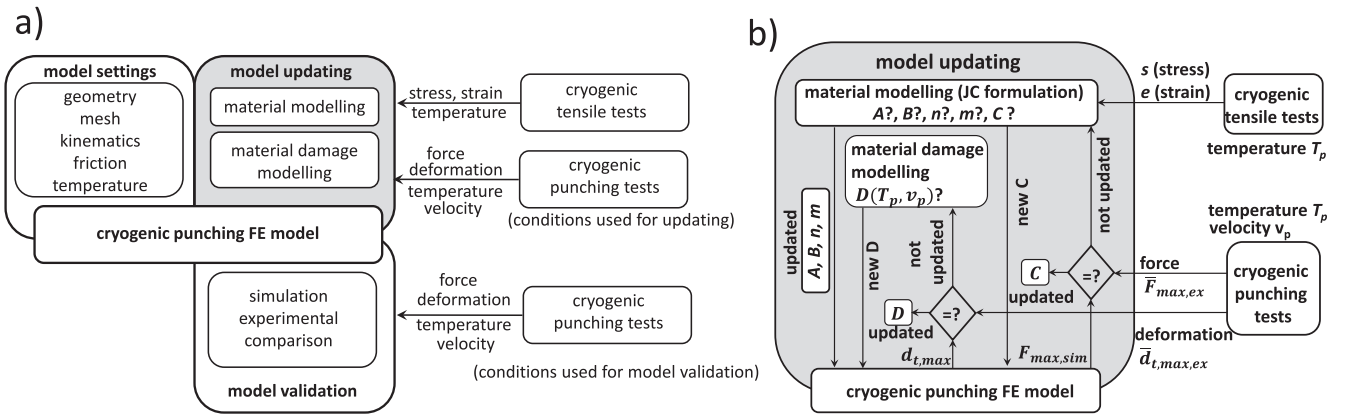

Fig. 4. model settings and model updating strategy overview a) material and damage modelling updating procedure b).

Design of experiments and equipment description

Tensile tests

As previously described in the Model Updating Strategy section, the tensile tests were carried out at five T_t temperatures: -80 °C, −60 °C, −40 °C, 0 °C and 20 °C.

For each temperature, three specimens were tested. According to ISO 6892-3 [44], a flat tensile test specimen with shoulders was used, Fig. 5 c). The specimen was characterized by a nominal cross-sectional area (6 mm (width) x 2.4 mm (thickness)) and a calibrated length equal to 25 mm. The specimens were manufactured through abrasive water jet technology starting from the same tube batch used for the piercing experimentation. In order to take into account the process accuracy and variability, the cross-sectional dimensions of each single specimen were measured. The MTS Alliance RF/150 tensile test machine, equipped with the MTS 651-environmental chamber, was used, Fig. 5. The machine has a thermal room able to reach different temperatures. In these tests the room was fed by nitrogen until the defined temperature is reached. The specimens to be tested at this temperature were positioned inside the chamber to reach the thermal equilibrium. To make the procedure faster and to ensure the achievement of the correct temperature, the specimens were immersed in a bath composed of liquid nitrogen and alcohol before being placed in the thermal chamber. The percentage of alcohol determines the temperature: a higher percentage results in a higher temperature. The temperature of the bath was monitored through a thermocouple.

The lowest temperature used in the experiment was selected according to the specifications of the environmental chamber. Indeed, the chamber can reliably achieve and maintain a stable temperature of −80 °C. Lower temperatures cannot be set with proper repeatability.

Although the ductile-to-brittle transition temperature depends on several factors (especially on loading rate [45,46]), −80 °C is expected to be adequately lower than the transition temperature for the adopted steel (S235JR). According to the specific literature ([47]), the transition temperature was estimated to be −12 °C. This estimation was made by the authors based on data from Charpy tests. It was anticipated during the experimental campaign design that the investigated temperature range would be suitable for observing the ductile-to-brittle transition, especially during the piercing tests where higher loading rates compared to tensile tests can be achieved.

The velocity of the crosshead that holds the specimens was equal to 4 mm/min, that corresponds to $\dot{\varepsilon}_0$. During the tensile tests, the crosshead position, the extensometer data (specimen extension) and the applied load were acquired with a time span of 0.1 s. The data were used to compute the nominal s and e.

Piercing tests

According to the defined model updating approach for the identification of both the C parameter (JC) and the damage material behaviour $D = D(v_p, T_p)$, it was necessary to perform piercing tests in different conditions both in terms of temperatures and piercing velocities. For this purpose, a 2-level factorial approach with a center point (intermediate conditions) was adopted. For each piercing condition, three repetitions were executed. The piercing tests were executed in randomized order. Table 2 resumes the tested conditions. The conditions used for updating

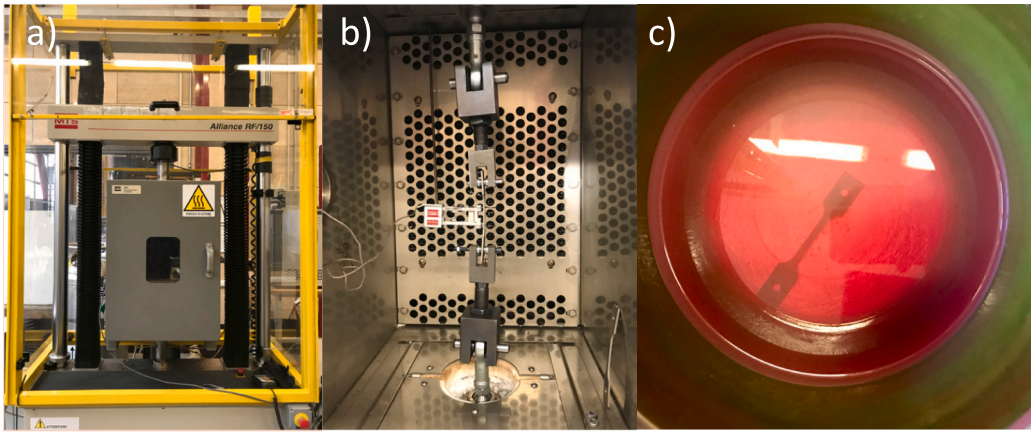

Fig. 5. a) Tensile test machine equipped with cryogenic chamber b) tensile test c) cryogenic bath and specimen.

Table 2
design of experiments – piercing tests.

Test condition ID	hydraulic unit HU	piercing velocity $v_p[mm/s]$	piercing temperature $T_p[^\circ C]$	updating parameter (measured quantity)
ID1	HU1	$v_{p,high}$	$T_{p,high}$	updating D($d_{t,max,ex}$), C($F_{max,ex}$)
ID2	HU1	$v_{p,high}$	$T_{p,mid}$	updating C($F_{max,ex}$)
ID3	HU1	$v_{p,high}$	$T_{p,low}$	updating D($d_{t,max,ex}$)
ID4	HU2	$v_{p,mid}$	$T_{p,high}$	validation
ID5	HU2	$v_{p,mid}$	$T_{p,mid}$	updating D($d_{t,max,ex}$)
ID6	HU2	$v_{p,mid}$	$T_{p,low}$	validation
ID7	HU3	$v_{p,low}$	$T_{p,high}$	updating D($d_{t,max,ex}$)
ID8	HU3	$v_{p,low}$	$T_{p,mid}$	validation
ID9	HU3	$v_{p,low}$	$T_{p,low}$	updating D($d_{t,max,ex}$)

the model and the ones used for the model validation were indicated, last column of Table 2.

More specifically, in accordance with the explanation provided in the previous section (and Fig. 4 b)), Table 2 describes the experimental data, reported in brackets, used for tuning the specific model parameter. The parameters tuning was considered achieved when the experimental/simulated matching was limited to a percentage error of about 3 %.

The piercing tests were carried out with the equipment schematized in Fig. 6 and described in Fig. 7. The dewar is connected to the tube to be processed through a vacuumed insulated pipe. The LN mass flow rate was tuned through the regulating valve (knob) that is installed on the dewar. A thermocouple was installed to continuously monitoring the temperature of the tube (see the details in Fig. 6 and Fig. 7 c)). Before doing the piercing, the valve was progressively opened until the targeted temperature T_p (piercing temperature), monitored through the thermocouple Fig. 7 c) was obtained. Once the steady-state condition was achieved, the piercing operation was performed. Such delivery solutions assured a homogeneous setting of the tube temperature. Moreover, the performed experiments revealed a high reproducibility piercing condition.

The actuator cylinder Fig. 7 a) and b) directly drives the punch through the pressurized oil provided by the hydraulic unit HU Fig. 7 a).

Three temperature levels were considered $T_{p,low} = -80^\circ C$, $T_{p,mid} = -40^\circ C$ and $T_{p,high} = 20^\circ C$.

To change the punching velocity v_p, three different hydraulic units were used, see Table 2. Since no detailed information about the hydraulic units had been available, an experimental characterization was carried out. Several air punching tests (without the tube) were executed to measure the average punching velocity. This was done exploiting an eddy current sensor that was installed to detect the punch motion.

From this experimental characterization it was found that respectively HU1 allowed to set a nominal (air) punching velocity $v_{p,high} = 731.4mm/s$, HU2 a punching velocity of $v_{p,mid} = 156.6mm/s$ and the HU3 a punching velocity of $v_{p,low} = 44.5mm/s$. Since each hydraulic unit has its own control unit and its dynamic properties, the real average punching velocities were also computed exploiting the experimental piercing data. It is worth of noting that the calculated real velocities and the maximum achievable pressures were properly set in the simulation FE model. As previously described, for both model updating and validation, the maximum punching force F_{max} and the maximum tube deflection $d_{t,max}$ were used.

The experimental punching force $F_{max,ex}$ was estimated measuring the cylinder inner pressure (pressure sensor, Fig. 7 a)) and knowing the cylinder area that is equal to 1256mm^2.

The tube deflection was measured scanning the upper tube area with Alicona infinite focus, see an example in Fig. 8.

For each tube, the $d_{t,max,ex}$ were measured. Since three repetitions were carried out for each piercing condition, the average values were computed ($\overline{d}_{t,max,ex}, \overline{F}_{max,ex}$).

For model validation purposes, an additional test was also carried out at $T_{p,low} = -80^\circ C$. In this test, performed with the HU1, the pressure threshold of the control unit was reduced to 160 bar in order to force a failure in the piercing process. Indeed, in such conditions, the punch should not be able to properly execute the tube piercing.

Results and discussion

In this section the main results in terms of material modelling characterization and cryogenic piercing modelling were reported.

First, the results obtained for the tensile tests performed at different temperatures were resumed in Fig. 9 and Fig. 10. Specifically, Fig. 9 shows respectively the R_{p02}, R_{p1} and the peak stress. For each quantity the 95 % confidence interval was also reported. Although the effect of the temperature on all the properties is clear evident, it can be observed that R_{p02} shows a higher variability while for R_{p1} and the peak stress the variance of the results is quite limited.

In Fig. 10, the Young's Module and the strain at break were also reported. It can be noted that both the quantities seem not strongly affected by the testing temperature.

As described in the Model updating strategy section, most of the JC parameters (A, B, n, m) were identified from the tensile test data. It's worth of noting that the A parameter was identified considering the R_{p1} value since this property exhibits a lower variability.

The found parameters were reported in Table 3. Fig. 11 a) shows the average curves got for experimental tensile tests performed at different temperatures. Fig. 11 b) shows the least square regression LSR (adopting Eq. (4)) carried out for estimating the m parameter. As a result of the material model updating, Fig. 12 shows the effect of the temperature on the identified JC model.

Regarding the Lathan Cockcroft model, the following formulation (Eq. (5)) was developed through a regression procedure that shows a $R^2 = 0.98$ and an adjusted value of $R^2_{adj} = 0.91$.

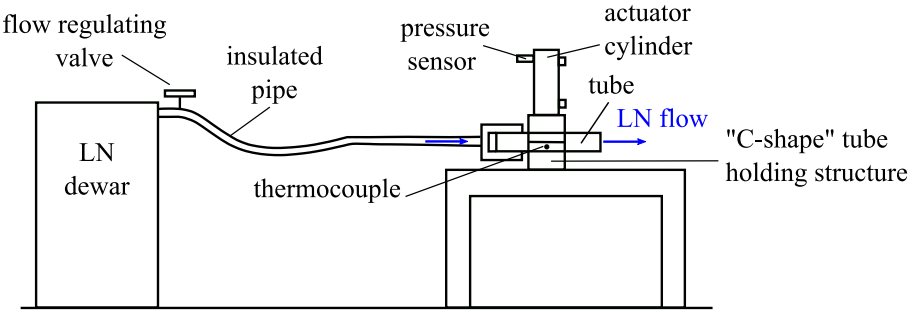

Fig. 6. experimental set up schematization.

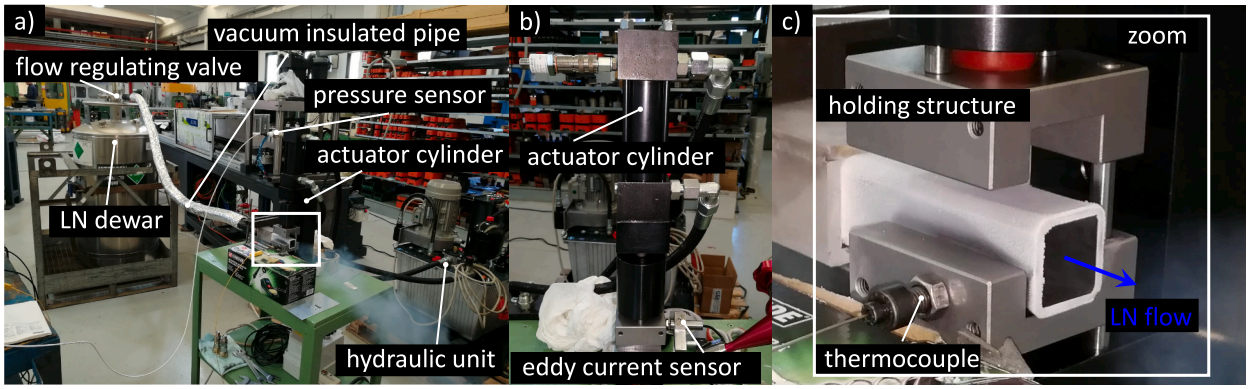

Fig. 7. a) experimental set up and sensors, b) actuator cylinder, c) process details and thermocouple for temperature measurements.

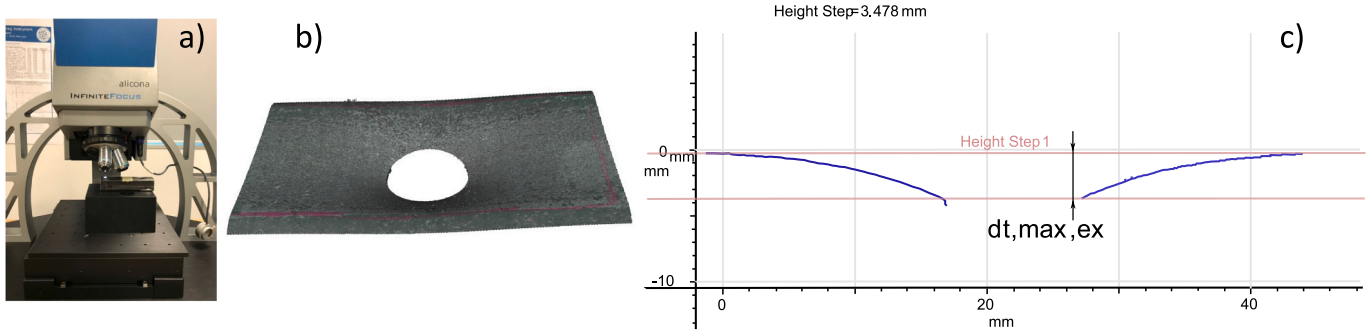

Fig. 8. Alicona a) upper tube scanning b) tube deflection measurement (longitudinal section) $d_{t,max,ex}$ b)

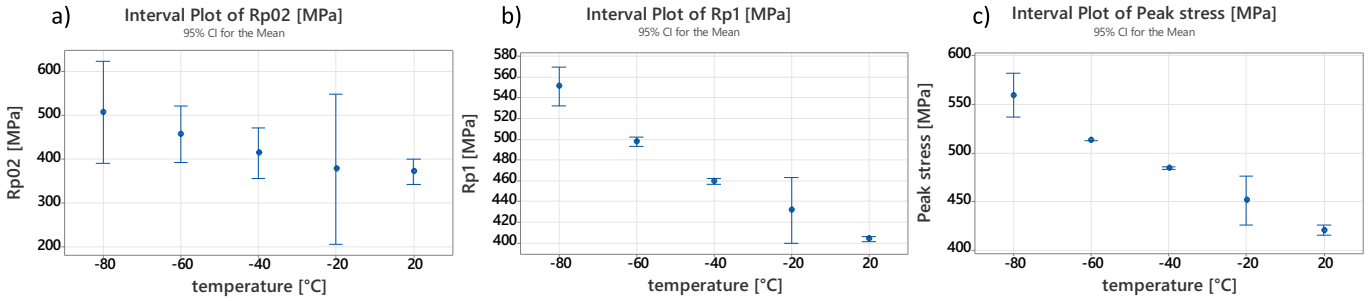

Fig. 9. Material (S235JR) properties as a function of the temperature a) R_{p02} b) R_{p1} c) Peak stress.

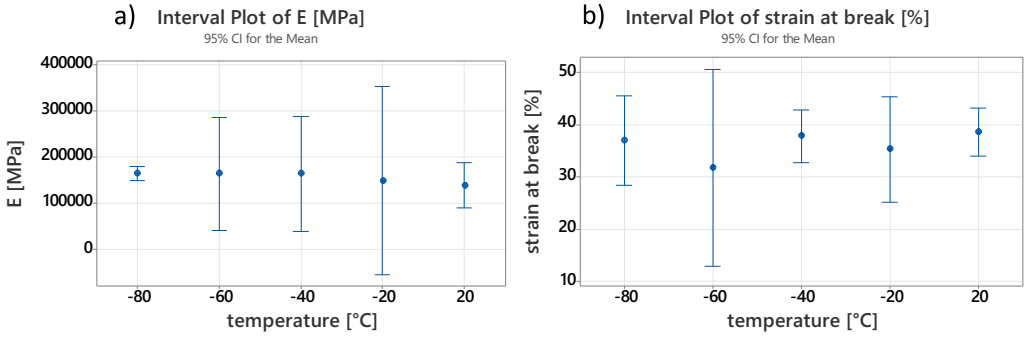

Fig. 10. Material (S235JR) properties as a function of the temperature a) Young's Module b) R_{p1} c) strain at break [%].

Table 3
JC identified model parameters (reference temperature − 80 °C).

A [MPa]	B [MPa]	n	C	m	$\dot{\varepsilon}_0[s^{-1}]$
460	150	0.1	0.045	0.53	0.002

$$D = D(v_p, T_p) = 0.831 - 0.000154 \bullet V_p + 0.003278 \bullet T_p + 2.761 \bullet 10^{-5} \bullet V_p \bullet T_p \quad (5)$$

Both the formulations (refer to Table 3 and Eq. (5)) were implemented in Forge to perform the piercing simulations. As anticipated in Table 2, some of the test conditions were used to calibrate the model according to the experimentally measured tube deflection and piercing force while some other test conditions were used to validate developed FE model. Among brackets were reported the updated numerical quantities. Table 4 resumes the main achieved results in the tested conditions. The percentage errors in both the maximum force $e_F = 100(F_{max,sim} - \overline{F}_{max,ex})/\overline{F}_{max,ex}$ and tube deflection estimation $e_d = 100(d_{t,max,sim} - \overline{d}_{t,max,ex})/\overline{d}_{t,max,ex}$ were reported. In addition, the real average punching velocities were also shown. As anticipated, they were computed for each HU and considering each specific punching conditions (ID). They were estimated analysing the experimental pressure profiles. It was found that the real punching velocities are much lower than the corresponding nominal ones (measured during air punching experiments) due to the dynamic behaviour of the HU and of its control unit under the effect of the piercing load.

It can be observed that the model reproduces the experimental data with a maximum error of 10 %, both on the punching force and tube deflection. This demonstrates that the developed material formulations, suitable for describing its behaviour at cryogenic temperatures, and the FE model can be considered rather accurate and can be used for predicting the wall deformation and the punching force involved in the process.

To better resume the effect of piercing temperature and velocity on experimental and simulated results in terms of maximum force and maximum tube wall deflection the following interaction plots were reported, see Fig. 13 and Fig. 14. It can be also appreciated that the numerical results mostly reproduce the experimental findings.

To further demonstrate the model potentialities, the additional test (piercing failure) was also numerically reproduced fictitiously setting a maximum force of 20kN in the FE model (corresponding to 160 bar). As can be observed in Fig. 15, the model can reproduce such additional case.

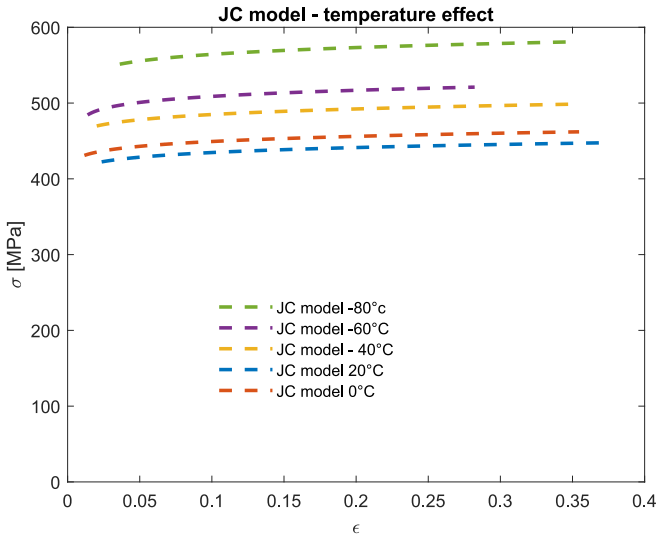

Fig. 12. identified JC model and effect of temperature.

The measurement of the average depth of the indentation left on the tube was carried out using a Keyence VHX 7000 (Fig. 15 c)). It was found that the average depth was 0.41 mm, while the numerical simulations showed a value of 0.35 mm, underestimating the depth by 15 %.

The developed model can be rather useful to design a new dieless punching system especially in the definition of its specifications in term of maximum punching force, punching velocity and punching temperature to be adopted.

Referring to the specific analysed case, considerations on the effect of the punching velocity and temperature can be carried out. Specifically, the temperature has a strong effect on both the punching force and on the maximum tube deflection, Fig. 13 and Fig. 14. It was found that averagely the punching force increases of about 20 % decreasing the T_p from 20 °C to −80 °C while the tube deflection decreases of about 29 %. The effect of the punching velocity is limited with respect to the one associated to the temperature. Its effect is more evident on the tube maximum deflection than on the punching force. This agrees with the literature findings, [33,34]. Moreover, it seems that the punching velocity shows its effect mainly at cryogenic temperatures (−80 °C).

This can be also appreciated in Fig. 14 where the spread of the data (effect of different punching velocities) seems increasing with the

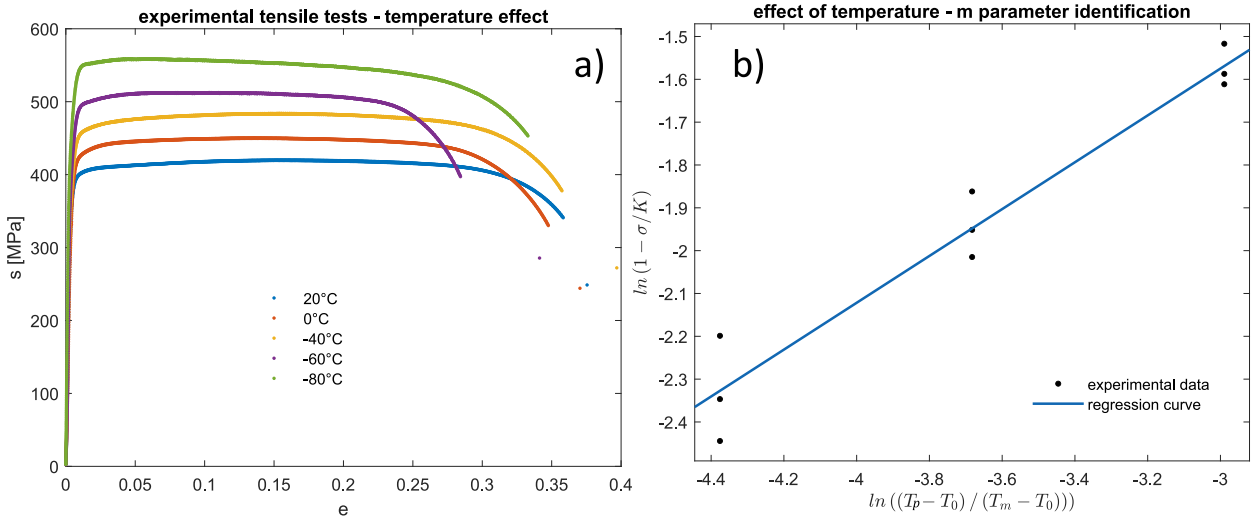

Fig. 11. effect of temperature: a) experimental tensile test data (average on three specimens) b) regression procedure for *m* parameter estimation.

Table 4
Experimental results and validation of the model.

ID	HU	v_p [mm/s]	T_p [°C]	$\bar{F}_{max,ex}$ [kN]	$F_{max,sim}$ [kN]	$\bar{d}_{t,max,ex}$ [mm]	$d_{t,max,sim}$ [mm]	e_F [%]	e_d [%]
ID1	HU1	137	20	23	(23.2)	3.95	(3.82)	(0.9)	(−3.3)
ID2	HU1	105	−40	25.1	(25.1)	3.48	3.38	(0)	−2.9
ID3	HU1	85	−80	28.6	27.4	2.79	(2.74)	−4.2	(−1.8)
ID4	HU2	20	20	22.2	22.23	3.92	(3.79)	0.1	(−3.3)
ID5	HU2	10	−40	25.3	24.4	3.89	3.53	−3.6	−9.3
ID6	HU2	4.5	−80	28.3	25.43	3.53	(3.44)	−10.1	(−2.5)
ID7	HU3	20	20	22.5	22.23	3.9	(3.79)	−1.2	(−2.8)
ID8	HU3	20	−40	25.7	24.9	3.55	(3.49)	−3.1	(−1.7)
ID9	HU3	20	−80	28	26.3	3.16	3.24	−6.1	2.5

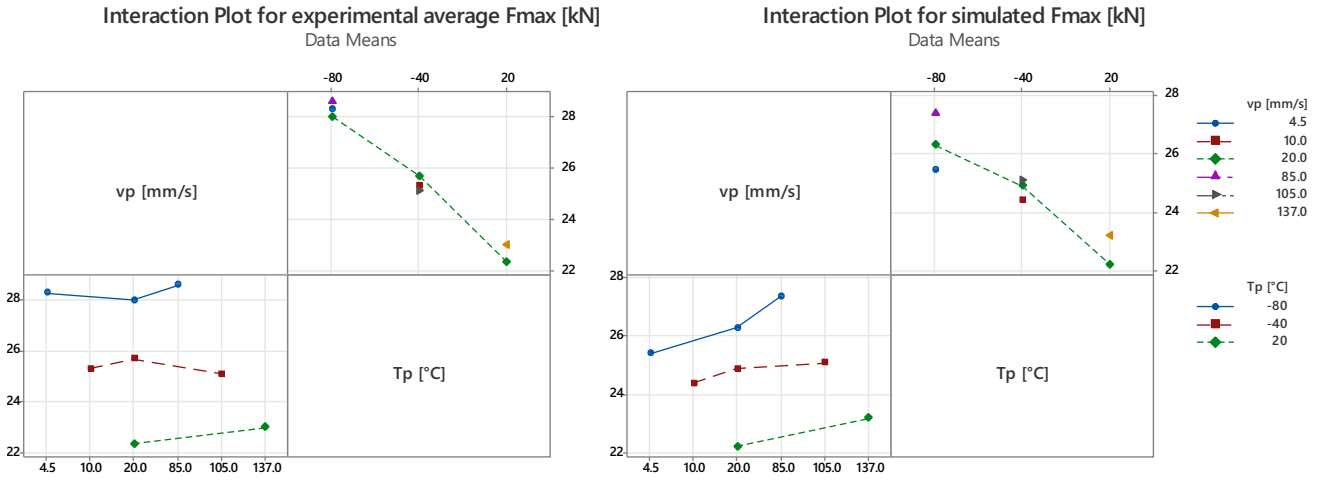

Fig. 13. Interaction plots for maximum punching force (experimental vs simulated).

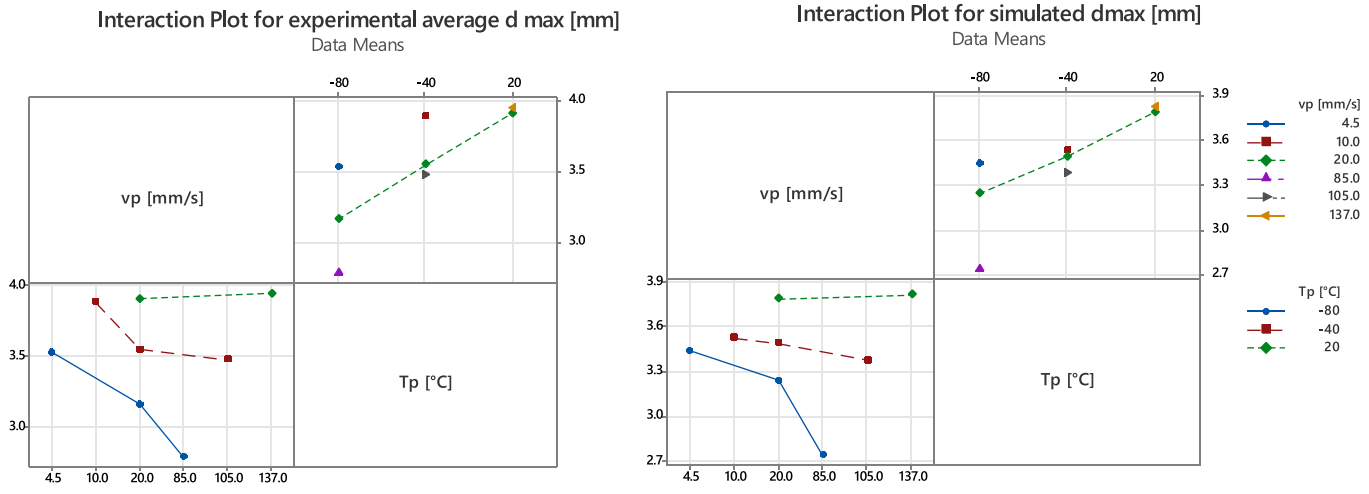

Fig. 14. Interaction plots for maximum tube deflection (experimental vs simulated).

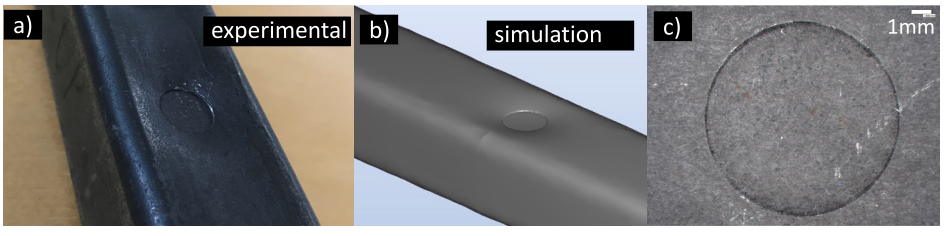

Fig. 15. Failed piercing test (experimental a) simulated results b) indentation measurement performed with Keyence VX 7000 c)) – model validation.

temperature reduction. The same effect was not appreciable in Fig. 13.

Indeed, in such conditions the deflection decreases of about 20 % if the punching velocity is increased from 4.5 mm/s to 85 mm/s. At −40 °C the tube deflection decreases of about 12 % increasing the punching velocity from 10 mm/s to 105 mm/s while at 20 °C the effect of the punching velocity seems negligible.

Ductile to brittle analysis

In this section an extensive analysis of the fracture behaviour of both tensile and piercing tests was carried out. The goal of the analysis was to check if the ductile-to-brittle transition really occurred in some of tested experimental conditions. Although the focus of the research was on the dieless cryogenic piercing process, the analysis was extended to the tensile tests. This was done to analyse the effect of the loading rate that is one of the most relevant parameters affecting the transition temperature.

The analysis was carried out adopting a threefold approach:

a) A Scanning Electrode Microscope SEM (Zeiss Evo) was used to analyse the occurred fractures. The images referring to the tests performed at different temperatures and in different conditions were compared and analysed with respect to analogous results found in literature.
b) The transition temperatures both for tensile and piercing tests were estimated exploiting the experimental data and a widespread formulation, e.g. Wallin and Baer [46] and in ASTM E2215 [48]. This allowed to better understand what happened during the tests.
c) The estimated transition temperatures were also verified using an empirical approach that allowed to consider the effect of the loading rate, e.g. Schindler et al. in [49] and Sreenivasan [50].

In Fig. 16, the fractures associated to tensile tests carried out respectively at ambient temperature (20 °C) and at −80 °C were compared at different magnifications. Although it can be observed some cracks in tests performed at −80 °C, the main part of the fracture region still shows a ductile behaviour.

The analysis was extended even considering the piercing tests. Fig. 17 resumes the SEM images of the following test conditions: ID2, ID3, and ID7 in Table 4. At different magnification ratios, the upper part of the picture refers to the test carried out at $T_p = 20^{\circ}C$ and with a puncing velocity $v_p = 20mm/s$, the intermediate ones are linked to the test performed at $T_p = -40^{\circ}C$ and $V_p = 105mm/s$ while the bottom ones are associated to the test carried out at the lowest temperature $T_p = -80^{\circ}C$ and at $V_p = 85mm/s$. According to the specific literature (e.g. Zeidi et al. [51]) the piercing fracture surface shows a rollover zone and a shear zone. The analysis was deepened focusing on the shear zone [51]: pictures at higher magnification ratios were collected for this purpose. Comparing the three images on the right, no relevant differences can be appreciated. Moreover, comparing the images with ductile and brittle fractures found in literature (e.g. Inoue et al. [52], Contreras et al. [53] and Perng et al. [54]) it can be concluded that no ductile-to-brittle transition occurred.

After having carried out the analysis of the fracture appearance at the SEM, the study was further extended focusing on the estimation of the transition temperatures. The goal of this second and third studies was to corroborate the above observations.

According to the specific literature (Wallin and Baer [46], ASTM E2215 [48]), one of the most adopted formulations for describing the behaviour of the fracture as a function of the testing temperature is the tanh function. In Eqs. (6) and (7) the tanh equations for both the tensile and the piercing tests were reported. The curves are typically used to estimate the transition temperatures from experiments. Specifically, in this work the respectively the transition temperature for the tensile tests T_{tran-t} and for the piercing tests T_{tran-p} were estimated through a nonlinear regression procedure. The regression procedure allowed to estimate even the half of the width of the transition region, respectively Q_t and Q_p. As suggested by [46] and Baer et al. [55], when only few data are available, the hypotheses reported in Eq. (8) can be adopted.

$$\varepsilon_{t-n} = \frac{US_t - LS_t}{2} \bullet \left(1 + tanh\left(\frac{T_p - T_{tran-t}}{Q_t}\right)\right) + LS_t \tag{6}$$

$$\varepsilon_{p-n} = \frac{US_p - LS_p}{2} \bullet \left(1 + tanh\left(\frac{T_p - T_{tran-p}}{Q_p}\right)\right) + LS_p \tag{7}$$

$$US_t = 1; US_p = \frac{\overline{\varepsilon}_p\left(T_p = 20^{\circ}C\right)}{\overline{\varepsilon}_t\left(T_p = 20^{\circ}C\right)}; LS_t = 0; LS_p = 0 \tag{8}$$

Since the absorbed energy data were not available, as suggested by Contrearas et al. in [53], Turba et al. in [56] and Altstadt et al. [57] that dealt with fracture properties in punching tests, they were substituted by the strain value at the failure region, see Eq. (9). The strain values (ε_t for the tensile and ε_p for the piercing) were computed analysing the thickness of the samples. For sake of completeness, Fig. 18 shows some measurements of the thickness (carried out using the microscope Keyence VX7000) in tensile test specimens and in the tube cross-sections. t_{tu_i} and t_{td_i} represent respectively the ith undeformed and deformed (after the fracture) thickness measurements of the tensile specimens.

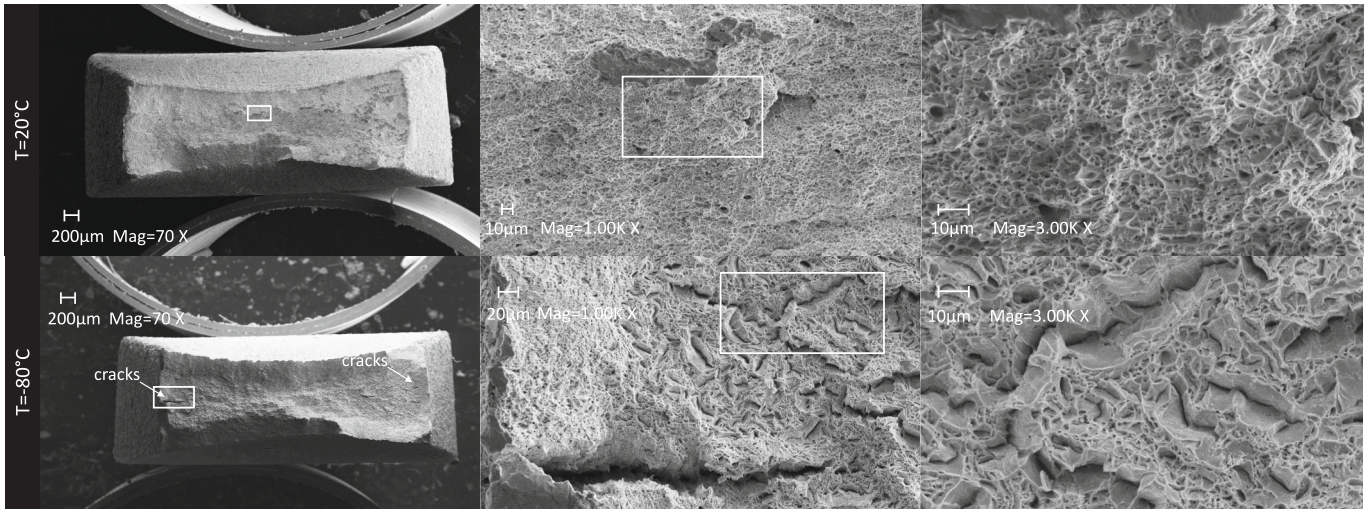

Fig. 16. Fracture analysis – tensile tests – SEM (different magnifications) – top 20 °C – bottom −80 °C.

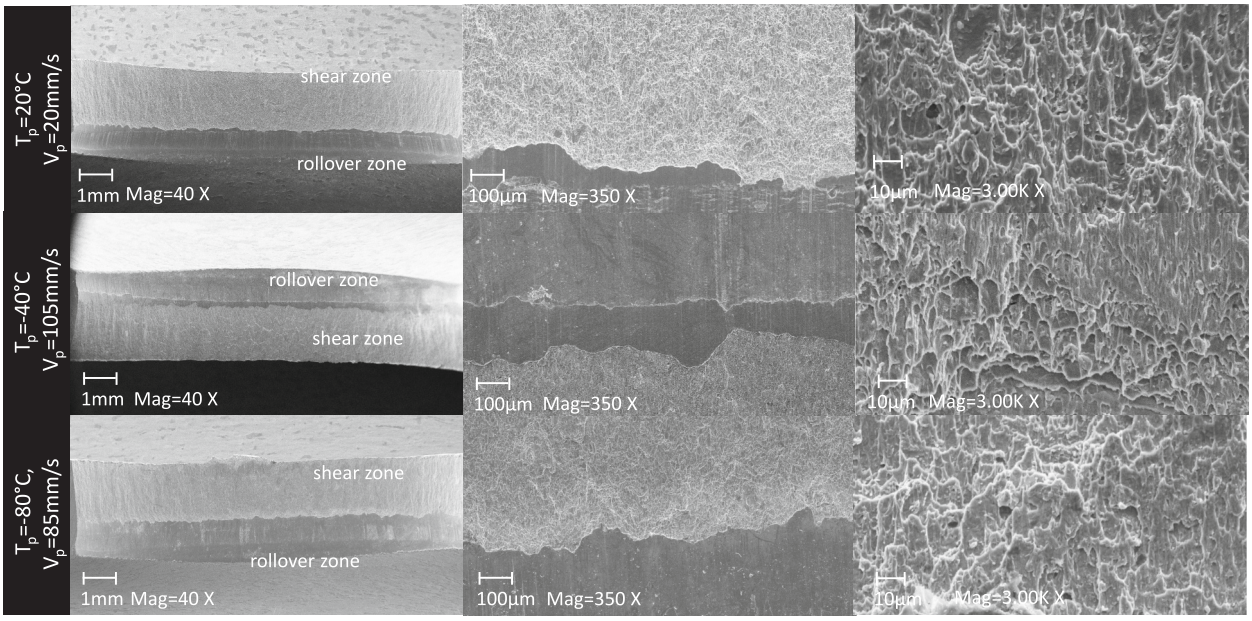

Fig. 17. Fracture analysis – piercing tests– SEM (different magnifications).

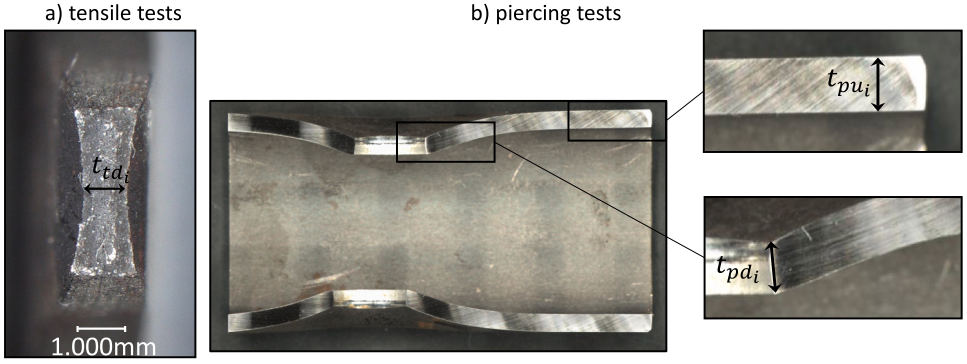

Fig. 18. Thickness analysis – a) example of fracture in tensile test b) piercing test (tube cross-section and details of the thickness measurements)

$$\varepsilon_t = ln\left(\frac{\bar{t}_{tu}}{\bar{t}_{td}}\right); \varepsilon_p = ln\left(\frac{\bar{t}_{pu}}{\bar{t}_{pd}}\right) \tag{9}$$

Similarly, t_{pu_i} and t_{pd_i} represent the ith measurement of the thickness respectively in the undeformed and deformed regions. The average values were computed through Eq. (10).

To consider in the same analysis both the tensile tests and the piercing tests, normalized strain values (ε_{t-n}, ε_{p-n}) were used, Eqs. (6)–(7) and Eq. (11). Referring to Eq. (8), $\bar{\varepsilon}_p\left(T_p = 20^\circ C\right)$ and $\bar{\varepsilon}_t\left(T_p = 20^\circ C\right)$ are respectively the mean of the ε_p and ε_t data available at $T_p = 20^\circ C$.

$$\bar{t}_{tu} = \sum_{i=1}^{5} t_{tu_i}; \bar{t}_{pu} = \sum_{i=1}^{5} t_{pu_i}; \bar{t}_{td} = \sum_{i=1}^{15} t_{td_i}; \bar{t}_{pd} = \sum_{i=1}^{5} t_{pd_i} \tag{10}$$

$$\varepsilon_{t-n} = \frac{\varepsilon_t}{\bar{\varepsilon}_t\left(T_p = 20^\circ C\right)}; \varepsilon_{p-n} = \frac{\varepsilon_p}{\bar{\varepsilon}_t\left(T_p = 20^\circ C.\right)} \tag{11}$$

The transition curves that fit the experimental data were reported in Fig. 19. It is worth of noting that all the data that refers to the tensile tests were exploited while the data linked to ID2, ID3 and ID 7 (piercing conditions reported in Table 4) were used for fitting purposes. Fig. 19 shows even the 90 % prediction bounds for both the curves.

In Table 5, the identified parameters of Eq. (6) and Eq. (7) were summarized, considering even their confidence intervals.

According to the found results (estimation of the transition temperatures), the analyses carried out through the SEM images were confirmed. Regarding the tensile tests, it was found that the transition temperature is much lower than −80 °C. This was expected since the load rate $\dot{K}$ that can be used in tensile tests is rather limited (medium-low values since the maximum load was reached within 12 s), see the definition provided in [45]. For what concerns the piercing tests, it was found that the transition temperature is close to the minimum experimented temperature (−80 °C). This was related to the fact that the observed loading rates were higher than the ones revealed in tensile tests but not as high as the expected due to the performance of the driving units. Indeed, as already noted, the measured punching velocities were considerably lower than the ones measured in air piercing. Although some of the piercing tests were executed in proximity of the transition temperature, no evidence of brittle transition was found. Barsom and Rolfe in [45] confirmed that in such a zone the fractural behaviour remains ductile.

In Table 6, the transition temperatures, associated to different tests, were reported. It allows observing the effect of the loading rate.

The estimation of the shift of the transition curves according to the

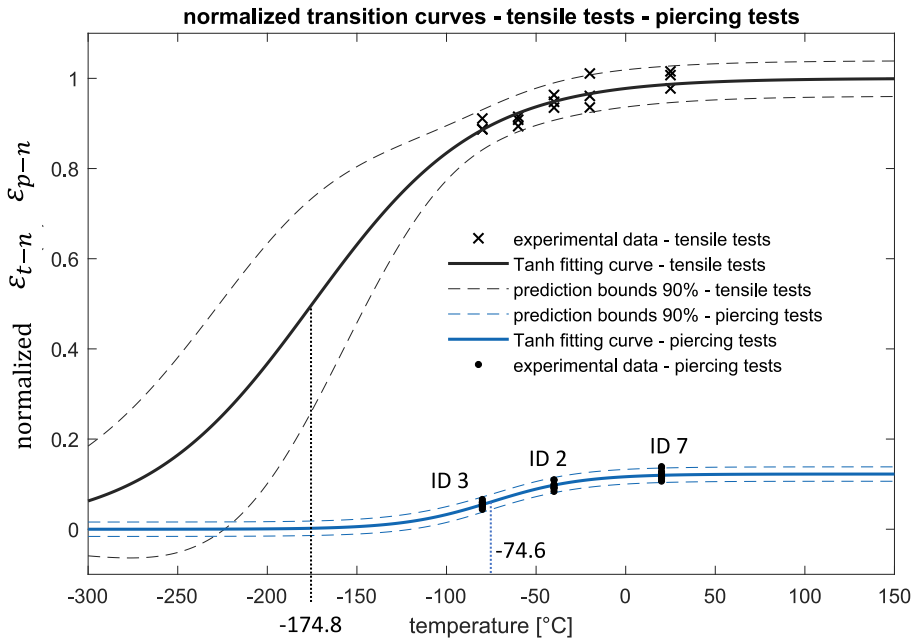

Fig. 19. Computed normalized transition curves – tensile tests and piercing tests.

Table 5
Identified parameters of the tanh equation both for tensile and piercing tests.

	Value	Confidence interval	Test
T_{tran-t} [°C]	−174.8	(−227.2, −122.5)	tensile
Q_t [°C]	92.56	(49.09, 136)	tensile
T_{tran-p} [°C]	−74.61	(−79.62, −69.59)	piercing
Q_p [°C]	50.11	(37.88,62.34)	piercing

Table 6
Transition temperature as a function of loading rate (S235JR).

	Charpy	piercing tests	tensile test
T_{tran} [°C]	−12	−74.6	−174.8
loading rate [mm/s]	5000 mm/s	4.5-137 mm/s	0.67 mm/s
source	literature	experimental/ modelling	experimental/ modelling

loading rate is still a challenging research topic. Several works can be found. Most of them proposes empirical formulations, for instance Schindler et al. in [49]. One of the most interesting approaches was developed by Wallin, as resumed in Sreenivasan [50]. The formulation allows to estimate the transition temperature in dynamic conditions through Eqs. (12) and (13). T_{p0} is the quasi static transition temperature, and A is the initial yield stress (Eq. (2), Table 3) stress at the reference temperature (20 °C), T_{p-dyn} is the transition temperature at higher loading rate $\dot{K}\left[MPa\sqrt{m}s^{-1}\right]$.

$$\Gamma = 9.9exp\left[\left(\frac{T_{p0}}{190}\right)^{1.66} + \left(\frac{A}{722}\right)^{1.09}\right] \tag{12}$$

$$T_{p-dyn} = \frac{T_{p0} \bullet \Gamma}{\left(\Gamma - ln\dot{K}\right)} \tag{13}$$

Exploiting the reported relationships, it was possible to numerically solving them and estimate T_{p0} for both the tensile tests and the piercing tests carried out in this work, starting from the literature data $T_{p-dyn} = -12^{\circ}C$, see Table 6. As suggested in Sreenivasan [50], the following values of $\dot{K}$ for the Charpy tests, the piercing tests and the tensile tests were respectively assumed: $\dot{K}_{Charpy} = 10^6[MPa\sqrt{m}s^{-1}]$, $\dot{K}_p = 5 \bullet 10^4[MPa\sqrt{m}s^{-1}]$ and $\dot{K}_t = 1[MPa\sqrt{m}s^{-1}]$.

The obtained estimation of the transition temperature for both tensile tests and piercing tests were respectively $T_{p0-t} = -180^{\circ}C$ and $T_{p0-p} = -71^{\circ}C$ that are very close to the ones estimated using the tanh fitting equations, see Table 6. This comparison validates the estimations performed even if carried out with a limited amount of data.

According to the performed analysis, it can be observed that the ductile-to-brittle transition was not properly occurred in all the experimental tests. Specifically, a piercing temperature close to −130 °C would be suggested to exploit such material transition. Even an increment of the piercing velocity would ease a further shift toward higher transition temperatures.

Conclusions

In this research, the use of cryogenics for dieless tube piercing was explored.

- Both experimental cryogenic punching tests and numerical simulations of the process were carried out. More in details, a FE model was developed and properly updated in terms of rheological material behaviour. For this purpose, both punching tests, executed at different temperatures and velocities, and tensile tests carried out at different velocities were executed. The experimental data (punching/piercing force and tube deformation) were used to identify the parameters of both the JC and LT models that feed the FE model.
- The estimating capabilities of the FE model were assessed considering some validation test conditions. The model showed quite good performances. Estimation errors lower than 10 % on the maximum punching force and maximum tube deflection were observed.
- It was noted that the punching velocity seems affecting the tube deformation only at cryogenic temperatures.
- Although the execution of the dieless punching at cryogenic temperatures (−80 °C) with the maximum achievable punching velocity (considering the equipment available in this research) allowed reducing the tube wall deformation, the result seems still much higher than the ones obtained with the regular tube punching

process. Indeed, in regular tube punching the maximum tube deflection is in the order of 0.3 mm that represents the extreme of the acceptable tolerance.

- A deep analysis on the observed fracture behaviour in both tensile tests and piercing tests was carried out exploiting SEM images. It was found that the ductile-to-brittle transition did not occur. Further verifications were also carried out estimating the transition temperatures through existing modelling approaches available in the specific literature.
- According to the described results, to make the cryogenic punching a feasible solution for piercing the tubes without the internal die, it would be necessary to investigate the performance even setting lower punching temperatures and especially imposing a much higher velocity to the punch. For this purpose, a specific punching control unit should be developed. An electric drive seems more adequate for the implementation of this innovative process.

Funding

The authors didn't receive any founds.

CRediT authorship contribution statement

Paolo Albertelli: Conceptualization, Data curation, Formal analysis, Methodology, Project administration, Software, Supervision, Validation, Writing – original draft, Writing – review & editing. **Michele Monno:** Supervision.

Declaration of competing interest

The authors declare that they have no known competing financial interests or personal relationships that could have appeared to influence the work reported in this paper.

Acknowledgments

The authors would thank Eng. Valerio Mussi and Eng. Davide Magnani for the support in the experimental activities. Special tanks even to Eng. Ludovica Rovatti and Eng. Michael Ishoa for the SEM analysis

References

[1] Jawahir IS, Attia H, Biermann D, Duflou J, Klocke F, Meyer D, et al. Cryogenic manufacturing processes. CIRP Ann Manuf Technol 2016;65:713–36. https://doi.org/10.1016/j.cirp.2016.06.007.
[2] Balaji V, Ravi S, Chandran PN, Damodaran KM. Review of the cryogenic machining in turning and milling process. Int J Res Eng Technol 2015;04:38–42. https://doi.org/10.15623/ijret.2015.0410008.
[3] Muhamad SS, Ghani JA, Che Haron CH. A review on future implementation of cryogenic machining in manufacturing industry. Progress in Industrial Ecology, An International Journal 2018;12:260–83. https://doi.org/10.1504/PIE.2018.097065.
[4] Shokrani A, Dhokia V, Muñoz-Escalona P, Newman ST. State-of-the-art cryogenic machining and processing. Int J Comput Integr Manuf 2013;26:616–48. https://doi.org/10.1080/0951192X.2012.749531.
[5] Madhukar S, Shravan A, Sai PV, Satyanarayana VV. A critical review on cryogenic machining of titanium alloy (TI-6AL-4V). Int J Mech Eng Technol 2016;7:38–45.
[6] Kaynak Y, Gharibi A. Cryogenic machining of titanium Ti-5553 alloy. J Manuf Sci Eng 2019;141:1–9. https://doi.org/10.1115/1.4042605.
[7] Kopac J, Pusavec F. Concepts of Sustainable Machining Processes. In: 13th International Research/Expert Conference "Trends in the Development of Machinery and Associated Technology"; 2009. p. 1–7.
[8] Pusavec F, Kopac J. Achieving and implementation of sustainability principles in machining processes. Advances in Production Engineering and Management 2009;4:151–60.
[9] Pusavec F, Kramar D, Krajnik P, Kopac J. Transitioning to sustainable production - part II: evaluation of sustainable machining technologies. J Clean Prod 2010;18:1211–21. https://doi.org/10.1016/j.jclepro.2010.01.015.
[10] Pusavec F, Krajnik P, Kopac J. Transitioning to sustainable production – part I: application on machining technologies. J Clean Prod 2010;18:174–84. https://doi.org/10.1016/j.jclepro.2009.08.010.
[11] Albertelli P, Monno M. Energy assessment of different cooling technologies in Ti-6Al-4V milling. Int J Adv Manuf Technol 2021;112:3279–306. https://doi.org/10.1007/s00170-020-06575-1.
[12] Gupta K, Laubscher RF. Sustainable machining of titanium alloys: a critical review. Proc Inst Mech Eng B J Eng Manuf 2017;231:2543–60. https://doi.org/10.1177/0954405416634278.
[13] Albertelli P, Strano M, Monno M. Simulation of the effects of cryogenic liquid nitrogen jets in Ti6Al4V milling. J Manuf Process 2023;85:323–44. https://doi.org/10.1016/J.JMAPRO.2022.11.053.
[14] Tahmasebi E, Albertelli P, Lucchini T, Monno M, Mussi V. CFD and experimental analysis of the coolant flow in cryogenic milling. Int J Mach Tool Manuf 2019;140:20–33. https://doi.org/10.1016/J.IJMACHTOOLS.2019.02.003.
[15] Salame C, Bejjani R. A better understanding of the cryogenic environment and the effect of nozzle location on the machinability of low carbon steel. J Manuf Process 2022;74:544–56. https://doi.org/10.1016/J.JMAPRO.2021.12.031.
[16] Rotella G, Umbrello D. Finite element modeling of microstructural changes in dry and cryogenic cutting of Ti6Al4V alloy. CIRP Ann Manuf Technol 2014;63:69–72. https://doi.org/10.1016/j.cirp.2014.03.074.
[17] Attanasio A, Ceretti E, Outeiro J, Poulachon G. Numerical simulation of tool wear in drilling Inconel 718 under flood and cryogenic cooling conditions. Wear 2020;458–459:43–1648. https://doi.org/10.1016/J.WEAR.2020.203403.
[18] Imbrogno S, Sartori S, Bordin A, Bruschi S, Umbrello D. Machining simulation of Ti6Al4V under dry and cryogenic conditions. Procedia CIRP 2017;58:475–80. https://doi.org/10.1016/j.procir.2017.03.263.
[19] Schreiber DK, Schwaiger R, Heilmaier M, McCormack SJ. Materials properties characterization in the most extreme environments. MRS Bulletin 2022 47:11 2022;47:1128–42. doi:https://doi.org/10.1557/S43577-022-00441-Z.
[20] Li X, Wei Z, Wang X, Yang L, Hao X, Wang M, et al. Effect of cryogenic temperatures on the mechanical behavior and deformation mechanism of AISI 316H stainless steel. J Mater Res Technol 2023;22:3375–86. https://doi.org/10.1016/J.JMRT.2022.12.190.
[21] Huang J. Microstructural effect on the ductile-to-brittle transitionin body centered cubic metals investigation by three dimensional dislocation dynamics simulations. University of California; 2004.
[22] Nam W, Hopperstad OS, Amdahl J. Modelling of the ductile-brittle fracture transition in steel structures with large shell elements: a numerical study. Marine Structures 2018;62:40–59. https://doi.org/10.1016/J.MARSTRUC.2018.07.003.
[23] Patil P, Tatet RG. Comparison of effects of cryogenic treatment on different types of steels: a review. Int J Comput Appl 2012;9:10–29.
[24] Siva RS, Mohan D, Jaswin MA, Sri Siva R, Mohan Lal D, Arockia Jaswin M. Optimization of Deep Cryogenic Treatment Process for 100Cr6 Bearing Steel Using the Grey-Taguchi Method55; 2012. p. 854–62. https://doi.org/10.1080/10402004.2012.720002.
[25] Reitz W, Pendray J. Cryoprocessing of materials: a review of current status. Materials and Manufacturing Processes 2006;16:829–40. https://doi.org/10.1081/AMP-100108702.
[26] Akincioğlu S, Gökkaya H, Uygur İ. A review of cryogenic treatment on cutting tools. Int J Adv Manuf Technol 2015;78:1609–27. https://doi.org/10.1007/S00170-014-6755-X/METRICS.
[27] Strano M, Albertelli P, Chiappini E, Tirelli S. Wear behaviour of PVD coated and cryogenically treated tools for Ti-6Al-4V turning. International Journal of Material Forming 2015:8. https://doi.org/10.1007/s12289-014-1215-6.
[28] Podgornik B, Paulin I, Zajec B, Jacobson S, Leskovšek V. Deep cryogenic treatment of tool steels. J Mater Process Technol 2016;229:398–406. https://doi.org/10.1016/J.JMATPROTEC.2015.09.045.
[29] Straffelini G, Bizzotto G, Zanon V. Improving the wear resistance of tools for stamping. Wear 2010;269:693–7. https://doi.org/10.1016/J.WEAR.2010.07.004.
[30] Yuan S, Cheng W, Liu W, Xu Y. A novel deep drawing process for aluminum alloy sheets at cryogenic temperatures. J Mater Process Technol 2020;284:116743. https://doi.org/10.1016/j.jmatprotec.2020.116743.
[31] Wang X, Fan X, Chen X, Yuan S. Forming limit of 6061 aluminum alloy tube at cryogenic temperatures. J Mater Process Technol 2022;306:117649. https://doi.org/10.1016/J.JMATPROTEC.2022.117649.
[32] Pineau A. Modeling ductile to brittle fracture transition in steels - micromechanical and physical challenges. Int J Fract 2008;150:129–56. https://doi.org/10.1007/S10704-008-9232-4/METRICS.
[33] Francois D, Pineau A. From Charpy to present impact testingvol. 30. ESIS Publication; 2002.
[34] Tvergaard V, Needleman A. An analysis of the temperature and rate dependence of Charpy V-notch energies for a high nitrogen steel. Int J Fract 1988;37:197–215. https://doi.org/10.1007/BF00045863/METRICS.
[35] Lei Sun Xu Z, Peng L, Lai X. Effect of grain size on the ductile-brittle fracture behavior of commercially pure titanium sheet metals. Mater Sci Eng A 2021;822:141630. https://doi.org/10.1016/J.MSEA.2021.141630.
[36] Sagar A, Nehme C, Saigal A, James TP. Stress–Strain Relationship of Polycaprolactone in Liquid Nitrogen for Finite Element Simulation of Cryogenic Micropunching Process. J Eng Sci Med Diagn Ther 2020:3. https://doi.org/10.1115/1.4047461.
[37] Sagar A, Nehme C, Saigal A, James TP. Cryogenic Material Properties of Polycaprolactone. In: ASME International Mechanical Engineering Congress and Exposition, Proceedings (IMECE); 2020. p. 3. https://doi.org/10.1115/IMECE2019-10180.
[38] Sagar A, Nehme C, Saigal A, James TP. Effect of die clearance on peak punching force during cryogenic micropunching of polycaprolactone. J Eng Sci Med Diagn Ther 2021:4. https://doi.org/10.1115/1.4049106.

[39] Mizumura M, Sato K, Kuriyama Y. Development of nut-inlaying technique in hydroformed component by hydro-burring. Mater Trans 2012;53:801–6. https://doi.org/10.2320/matertrans.MF201105.
[40] Keum YT, Wagoner RH, Lee JK. Friction model for FEM simulation of sheet metal forming operations. In: AIP conference proceeding 712. AIP Publishing; 2004. p. 989–94. https://doi.org/10.1063/1.1766656.
[41] Albertelli P, Strano M, Monno M. Simulation of the effects of cryogenic liquid nitrogen jets in Ti6Al4V milling. J Manuf Process 2023;85:323–44. https://doi.org/10.1016/J.JMAPRO.2022.11.053.
[42] Nasri MT, Abbassi F, Ahmad F, Makhloufi W, Ayadi M, Mehboob H, et al. Experimental and numerical investigation of sheet metal failure based on Johnson-cook model and Erichsen test over a wide range of temperatures. Mechanics of Advanced Materials and Structures 2023;30:2087–100. https://doi.org/10.1080/15376494.2022.2049934.
[43] Schwab R, Harter A. Extracting true stresses and strains from nominal stresses and strains in tensile testing. Strain 2021:57. https://doi.org/10.1111/STR.12396.
[44] ISO 6892-3. Metallic Materials - Tensile testing - part 3. 2015.
[45] Barsom JM, Rolfe ST. Fracture and fatigue control in structures applications of facture mechanics. 3rd ed. 1999. Woburn, MA.
[46] Wallin K, Baer W. Evaluation of Charpy-V transition curve fitting based on distribution-free statistical assessment. International Journal of Pressure Vessels and Piping 2023;206:105079. https://doi.org/10.1016/J.IJPVP.2023.105079.
[47] Lacalle R, Álvarez JA, Ferreño D, Portilla J, Ruiz E, Arroyo B, et al. Influence of the flame straightening process on microstructural, mechanical and fracture properties of S235 JR, S460 ML and S690 QL structural steels. Exp Mech 2013;53:893–909. https://doi.org/10.1007/s11340-013-9723-8.
[48] ASTM E2215. Standard Practice for Evaluation of Surveillance Capsules from Light- Water Moderated Nuclear Power Reactor Vessels. 2019.
[49] Schindler HJ, Kalkhof D. A closer look at effects of the loading rate on fracture toughness in the ductile-to-brittle transition regime of a ferritic steel. J Test Eval 2015;43:507–16. https://doi.org/10.1520/JTE20120321.
[50] Sreenivasan PR. Inverse of Wallin's relation for the effect of strain rate on the ASTM E-1921 reference temperature and its application to reference temperature estimation from Charpy tests. Nuclear Engineering and Design 2011;241:67–81. https://doi.org/10.1016/j.nucengdes.2010.09.035.
[51] Zeidi A, Ben Saada F, Elleuch K, Atapek H. On the failure of punching process. Eng Fail Anal 2021:120. https://doi.org/10.1016/j.engfailanal.2020.105035.
[52] Inoue T, Qiu H, Ueji R, Kimura Y. Ductile-to-brittle transition and brittle fracture stress of ultrafine-grained low-carbon steel. Materials 2021:14. https://doi.org/10.3390/ma14071634.
[53] Contreras MA, Rodríguez C, Belzunce FJ, Betegón C. Use of the small punch test to determine the ductile-to-brittle transition temperature of structural steels. Fatigue Fract Eng Mater Struct 2008;31:727–37. https://doi.org/10.1111/j.1460-2695.2008.01259.x.
[54] Peng W, Zhang J, Yang X, Zhu Z, Liu S. Failure analysis on the collapse of leaf spring steels during cold-punching. Eng Fail Anal 2010;17:971–8. https://doi.org/10.1016/j.engfailanal.2009.11.008.
[55] Baer W, Wossidlo P, Abbasi B. On the question of how to analyze and apply Charpy pendulum impact test results correctly - shortcomings in corresponding procedures and standards. J Test Eval 2022:50. https://doi.org/10.1520/JTE20210781.
[56] Turba K, Gülçimen B, Li YZ, Blagoeva D, Hähner P, Hurst RC. Introduction of a new notched specimen geometry to determine fracture properties by small punch testing. Eng Fract Mech 2011;78:2826–33. https://doi.org/10.1016/j.engfracmech.2011.08.014.
[57] Altstadt E, Bergner F, Houska M. Use of the small punch test for the estimation of ductile-to-brittle transition temperature shift of irradiated steels. Nuclear Materials and Energy 2021:26. https://doi.org/10.1016/j.nme.2021.100918.

Paolo Albertelli has been developing his research activities as an Assistant Professor of the Mechanical Engineering Department of Politecnico di Milano. His research has been focused mainly on the development of Advanced Manufacturing Solutions and Manufacturing Processes Sustainability. Regenerative chatter modelling, cutting stability prediction, chatter monitoring, vibration suppression and the development of advanced monitoring solutions are some of the covered topics. His research is even focused on Energy consumption (assessment, identification, modelling and reduction) in Machine Tools. Moreover, he is working on cryogenics as a feasible and sustainable solution for machining hard to cut materials and for some forming processes.

Michele Monno, His scientific activity was initially focused on pure waterjet (WJ) and abrasive waterjet (AWJ) technologies, electro-discharge machining (EDM) and high-definition plasma (HDP). Since 2006 the research activity has been addressed to the improvement of machine tools performance with a new facility, the MUSP Laboratory, in Piacenza. Among the research activities, developed in recent years in cooperation with companies, the study of metal foam filling to improve the dynamic behaviour of machine tools structures and the research on production processes for metal foam/sponges; the substitution of lubricant fluids in metal cutting with liquid nitrogen (for titanium alloys machining).